



Three-dimensional optical trapping and orientation of microparticles for coherent X-ray diffraction imaging

Yuan Gao^{a,b,1}, Ross Harder^c, Stephen H. Southworth^a, Jeffrey R. Guest^d, Xiaojing Huang^b, Zijie Yan^{e,f}, Leonidas E. Ocola^d, Yuval Yifat^e, Nishant Sule^e, Phay J. Ho^a, Matthew Pelton^g, Norbert F. Scherer^{d,e,h}, and Linda Young^{a,e,i,1}

^aChemical Sciences & Engineering Division, Argonne National Laboratory, Lemont, IL 60439; ^bNational Synchrotron Light Source II, Brookhaven National Laboratory, Upton, NY 11973; ^cAdvanced Photon Source, Argonne National Laboratory, Lemont, IL 60439; ^dCenter for Nanoscale Materials, Argonne National Laboratory, Lemont, IL 60439; ^eJames Franck Institute, The University of Chicago, Chicago, IL 60637; ^fDepartment of Chemical and Biomolecular Engineering, Clarkson University, Potsdam, NY 13699; ^gDepartment of Physics, University of Maryland, Baltimore County (UMBC), Baltimore, MD 21250; ^hDepartment of Chemistry, The University of Chicago, Chicago, IL 60637; and ⁱDepartment of Physics, The University of Chicago, Chicago, IL 60637

Edited by A. Paul Alivisatos, University of California, Berkeley, CA, and approved January 3, 2019 (received for review November 29, 2017)

Optical trapping has been implemented in many areas of physics and biology as a noncontact sample manipulation technique to study the structure and dynamics of nano- and mesoscale objects. It provides a unique approach for manipulating microscopic objects without inducing undesired changes in structure. Combining optical trapping with hard X-ray microscopy techniques, such as coherent diffraction imaging and crystallography, provides a nonperturbing environment where electronic and structural dynamics of an individual particle in solution can be followed in situ. It was previously shown that optical trapping allows the manipulation of micrometer-sized objects for X-ray fluorescence imaging. However, questions remain over the ability of optical trapping to position objects for X-ray diffraction measurements, which have stringent requirements for angular stability. Our work demonstrates that dynamic holographic optical tweezers are capable of manipulating single micrometer-scale anisotropic particles in a microfluidic environment with the precision and stability required for X-ray Bragg diffraction experiments—thus functioning as an “optical goniometer.” The methodology can be extended to a variety of X-ray experiments and the Bragg coherent diffractive imaging of individual particles in solution, as demonstrated here, will be markedly enhanced with the advent of brighter, coherent X-ray sources.

optical tweezers | coherent X-ray diffraction imaging | microfluidic | optical trapping | nanoscience

Coherent X-ray diffraction imaging (CXDI) is a powerful, elegant, and rapidly developing technique that enables structure determination of noncrystalline samples to a resolution limited only by the wavelength of the X-rays and largest scattering angles measured (1–4). The continuing development of CXDI methods (5) has been spurred by the revolution in sources of ultrabright coherent X-ray radiation [synchrotrons, free-electron lasers (FELs), and high harmonic generation (HHG)] (6–8). Following the first proof-of-principle demonstration in two dimensions using coherent, spatially filtered synchrotron radiation, where the structure of an engineered micrometer-scale target was reconstructed using an oversampled X-ray diffraction pattern and phase retrieval (1), analogous demonstrations using FELs (9) and tabletop HHG radiation (10) were realized. Going beyond fabricated 2D targets, there has been considerable work on naturally occurring biological samples (2, 11, 12) and single-particle imaging in 2D (13) and 3D (14, 15) using the diffract-before-destroy methodology (16) in the original forward scattering geometry.

CXDI in the Bragg geometry, where coherent scattering around a Bragg peak is recorded, has developed concurrently and with considerable impact for materials science. With Bragg CXDI one is able to recover the 3D shape and strain structure from nanoparticles (17–21). The exquisite sensitivity to strain at the picometer level makes Bragg CDI sensitive to defects (20) and structural changes due to chemical reaction at strained sites (22). Being able to monitor an isolated particle in solution as it undergoes interaction with the solvent or other reactants with

the high spatial and temporal resolution that is possible with Bragg CXDI would likely have wide-ranging applications (23). Typically, Bragg CXDI has been performed with nanocrystals firmly affixed by chemical or other means to a solid substrate (15–18). This method of sample fixing and manipulation has been shown to modify the local strain (21) and simply will not allow monitoring the evolution of a free “isolated” particle in solution.

Here we demonstrate a method, based on dynamic holographic optical trapping in a standing-wave geometry, to hold and manipulate a single nanoscale particle in solution with sufficient angular stability to perform Bragg CXDI and thus obtain 3D maps of shape and strain for a single particle suspended in solution. Optical tweezers (OTs) have been previously used in many fields for non-contact sample manipulation (24–27) and more recently for X-ray characterization experiments (28–30). Two of these OTs/X-ray implementations utilize, as we do here, a spatial light modulator (SLM) to generate multiple foci (28, 29). However, while expressing interest, those studies have not reported angular control as one would have with a standard, mechanical goniometer. Here, because of the standing-wave geometry (31, 32), we are able to exert the requisite control and achieve the stringent angular stability required for Bragg CDI.

Significance

Obtaining a fundamental understanding of crystal growth and chemical reactions in solution is of broad and enduring interest for materials discovery, structural biology, and catalysis. The recent availability of bright, coherent X-ray sources can enable these fluctuation-driven processes to be monitored in situ through the technique of coherent X-ray diffractive imaging (CXDI), in which the 3D internal structure of microscopic objects is determined with nanometer resolution from the fine structure of diffraction peaks. So far, Bragg CXDI has required immobilization of particles on a substrate, which modifies their structure and chemical activity. Here, we demonstrate Bragg CXDI on a single particle that is trapped and oriented in solution using optical tweezers and thus obtain its 3D structure and strain map.

Author contributions: M.P., N.F.S., and L.Y. conceived the project; Y.G., J.R.G., and Z.Y. built and optimized the optical trapping apparatus; Y.G. and L.E.O. fabricated the microfluidic sample cells; Y.G., R.H., S.H.S., and N.F.S. planned and executed the X-ray diffraction experiments; Y.G., Y.Y., N.S., and P.J.H. conducted the simulations; Y.G. and X.H. performed the analysis of coherent X-ray diffraction data; and Y.G., M.P., N.F.S., and L.Y. wrote the paper with input from all coauthors.

The authors declare no conflict of interest.

This article is a PNAS Direct Submission.

Published under the PNAS license.

¹To whom correspondence may be addressed. Email: yuangao@bnl.gov or young@anl.gov.

This article contains supporting information online at www.pnas.org/lookup/suppl/doi:10.1073/pnas.1720785116/-DCSupplemental.

This combination of Bragg CDI with the dynamic holographic OTs is ideal for characterizing our sample, an individual micrometer-long nanowire. Nanowires are often used as key elements for light generation, propagation, and detection in nanoscale photonic circuits (33, 34). While often considered defect-free (35, 36), nanowires have recently been shown to have structural inhomogeneities such as stacking faults and twinning planes that can significantly affect their optical behavior (37–39) and are thus interesting candidates for noncontact Bragg CXDI. Moreover, because the stability and angular control required for Bragg CXDI exceeds that required for other X-ray imaging techniques—such as X-ray fluorescence imaging and tomography—we anticipate our noncontact optical goniometer to be readily adaptable for X-ray imaging of individual particles in solution.

Results and Discussion

Multifocus Standing-Wave Optical Trap. We use a standing-wave optical configuration (31) to obtain a high-stiffness 3D optical trap (Fig. 1). Traditional single-beam OTs are more straightforward to employ for 2D than for 3D manipulation due to the requirement to balance gradient and scattering forces (40). Provided that the index of refraction of the trapped object is larger than the surrounding medium, the gradient force, proportional to the gradient of the electric-field intensity, attracts the object to the center of the laser focus, while the scattering force repels the object. Because of the relatively small electric-field gradient along the longitudinal direction of the laser focus in the single-beam OTs, the scattering force is difficult to counteract along the laser propagation direction, resulting in an axially loose trap.

In our experiment, we combined a holographic beam-shaping technique and an in situ-deposited micromirror to generate the standing wave. Unlike our previous work (32) that utilized a Bessel beam to form a standing wave very close to the surface of the mirror, we utilized a binary zone plate phase mask on the SLM. The combination of a binary zone plate and an in situ mirror allows the generation of a standing-wave focus tens of microns away from the mirror surface and also permits the adjustment of the trap position along the laser propagation direction. This distance can be tuned accurately and is limited only by the resolution

of the phase pattern displayed on the SLM (*SI Appendix*), and therefore the trapped particle can be manipulated precisely in 3D.

Multiple standing-wave foci can be formed simultaneously and be manipulated independently by random mask encoding (41). While a mesoscopic particle is held by such a multifocus trap, we can accurately control its 3D position and angular orientation by independently adjusting the alignment of the foci. As shown in Fig. 1*A*, a cylindrically shaped particle is trapped by two standing-wave foci, with each focus holding one end of the particle. The particle can be freely aligned by changing the positions of the two standing-wave foci in 3D. In particular, by moving the foci along the laser propagation direction (i.e., y axis), the particle can be tilted with sub-milliradian accuracy. This has never been achieved with single-beam OTs. *Movie S1* demonstrates the precise control of the tilting angle of a single ZnO microparticle by adjusting the phase of the laser (see Fig. 1*C* for the diffraction geometry). The movie shows that a Bragg diffraction peak, which was otherwise partially blocked by the sample cell, can be viewed in full by adjusting the phase mask displayed on the SLM.

Stability of Optically Aligned Anisotropic Objects. Before attempting a Bragg CXDI measurement, the angular fluctuations of the trapped particle were measured in each dimension to quantitatively evaluate the trapping stability. For our experiments, we chose cylindrically shaped crystalline ZnO particles as the sample. The ZnO particles are typically 0.5 to 1 μm in diameter and 10 to 20 μm in length with a wurtzite lattice and hexagonal cross-section. The refractive index of ZnO is 1.94 (42), in comparison with 1.33 for the water solvent. Particles were trapped and aligned by the dual-foci standing-wave trap (as shown in Fig. 1*A*). The trapping stability was determined by observing the Bragg diffraction from the [002] lattice planes, which are normal to the long axis of the cylindrically shaped particle.

Due to the limited aperture of the sample cell, the particles were aligned to diffract in the horizontal plane. As shown in Fig. 1*C*, the three rotational axes are defined in the coordinate frame of the particle (i.e., x' , y' , and z'). The angular stability of the

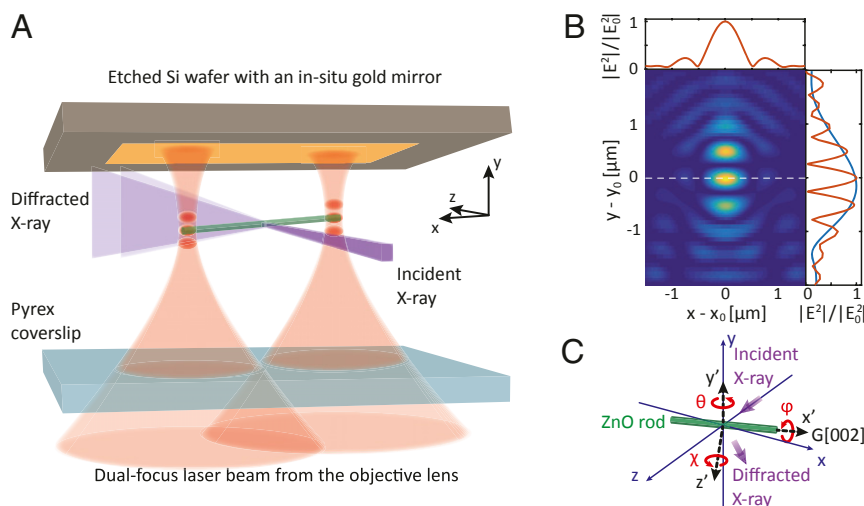


Fig. 1. Schematic diagram of the experiment. (A) A mesoscopic cylindrically shaped ZnO particle is aligned by two standing-wave foci. The laboratory coordinates are defined as x , outboard; y , upward; and z , downstream of the X-ray beam. (B) Simulated electric-field intensity $|E^2|$ of a standing-wave focus. Bottom left: Two-dimensional plot of the electric-field intensity in the x - y plane, where the laser propagates to the positive y direction. Bottom right: The electric-field intensity $|E^2|$ along the axis of the laser beam ($x - x_0 = 0$) of a standing-wave focus (red) and a simple Gaussian beam focus (blue), calculated by FDTD. Top: The electric-field intensity $|E^2|$ of the standing-wave focus along the dashed line in the 2D plot. (C) A schematic of the diffraction geometry. The ZnO particle is aligned in the x - z plane of the laboratory coordinates. The X-ray beam is incident along the z axis and then diffracts to the outboard direction. The reciprocal lattice vector $G[002]$ is along the long axis of the particle. φ , θ , and χ describe the angular positions around the three rotational axes defined in the coordinate frame of the particle, where φ is around x' , the long axis of the cylindrically shaped particle; θ is around y' , the vertical axis; and χ is around z' , the orthogonal axis. Details of the multifocus beam and phase function on the SLM are given in *SI Appendix, Fig. S1*. Details of the sample cell are given in *SI Appendix, Fig. S2*.

trapped particle can be characterized by the corresponding angular variances $\langle(\Delta\varphi)^2\rangle$, $\langle(\Delta\theta)^2\rangle$, and $\langle(\Delta\chi)^2\rangle$. Due to the diffraction geometry in our experiment, the measurement is least sensitive to $\langle(\Delta\varphi)^2\rangle$. Therefore, we will discuss $\langle(\Delta\theta)^2\rangle$ and $\langle(\Delta\chi)^2\rangle$ first.

$\langle(\Delta\theta)^2\rangle$ is characterized by measuring the FWHM of the rocking curve. In our experiment, since the illuminated section of crystal was less than a few microns in size, the natural width of the [002] diffraction peak was much larger compared with the energy and angular widths of the incident X-ray beam. Therefore, the FWHM of the rocking curve was a convolution of the natural width of the diffraction peak and the broadening induced by the angular fluctuations of the particle (as shown in Fig. 2A).

However, since the trapped ZnO particle was not necessarily a single crystal, the X-rays could be diffracted by a crystalline grain that was even smaller than the illuminated part of the particle. Therefore, the natural width of the Bragg peak was a priori unknown in our experiment. We scanned the rocking curve of a particle multiple times at different laser powers to determine the natural width of the diffraction peak. If we assume that there was no radiation-induced structural change during the measurement, the differences in the FWHM of the rocking curves resulted from the change of the angular fluctuations with laser power. Based on the equipartition theorem, $\langle(\Delta\theta)^2\rangle$ can be written as

$$\langle(\Delta\theta)^2\rangle = \frac{2k_B T}{\kappa D^2}, \quad [1]$$

where D is the distance between the two Gaussian foci, k_B is the Boltzmann constant, T is the temperature of the particle, and κ is

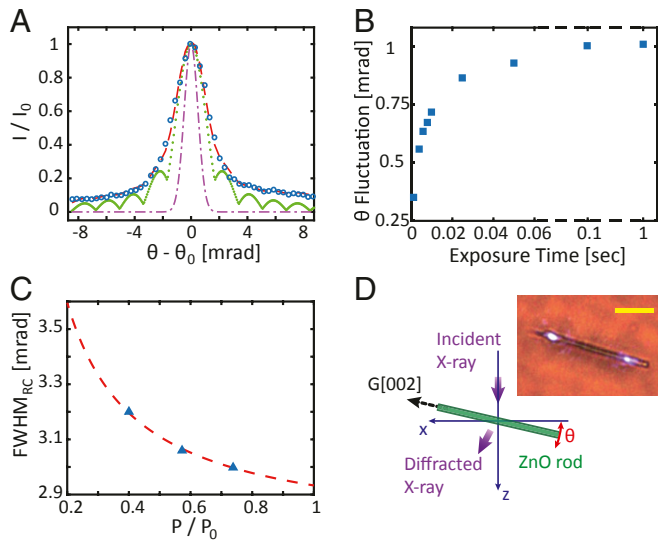


Fig. 2. Angular stability around the y' axis. (A) Rocking curve measured from a $\sim 15\text{-}\mu\text{m}$ -long ZnO particle trapped by two standing-wave foci located $12\ \mu\text{m}$ apart. The image of the trapped particle is shown in D, Inset. The measured rocking curve of the Bragg peak (open circle) with 3.0-mrad FWHM is fitted (dashed red line) as the convolution between the coherent diffraction from a $\sim 70\text{-nm}$ -size ZnO crystal (dotted green line) and the distribution of the particle's angular displacement in θ (dashed-dotted magenta line). (B) Calculated distribution of the trapped cylindrical shape particle's angular displacement for different exposure times. (C) FWHM of the rocking curve measured from the same particle at three different laser powers (filled triangle). Since the distribution of the angular displacement is proportional to $(I_{\text{Laser}})^{-1/2}$, the rocking curve's FWHM is a function of the laser power (dashed curve). (D) A schematic of the diffraction geometry (view from bottom to top). The ZnO rod was rotated in the x - z plane to scan the rocking curve. (Inset) Bright-field image of the measured ZnO rod trapped by two laser foci (bright spots near the ends of the rod). This image was obtained with the same microscope objective that focused the laser. (Scale bar: $5\ \mu\text{m}$.)

the translational trapping stiffness in the z' direction, which is proportional to the laser intensity, I_{Laser} . Details of the derivation are given in *SI Appendix*. From Eq. 1 we can see that the angular displacements in θ are described by a Gaussian distribution with an FWHM $\propto \kappa^{-1/2} \propto (I_{\text{Laser}})^{-1/2}$. The angular fluctuations are also proportional to D^{-1} , indicating that a longer trapped rod has smaller angular fluctuations since the laser foci can be further apart.

To fully evaluate the broadening of the rocking curve due to the angular fluctuations, we simulated the motion of an optically trapped cylindrically shaped object in a medium with the friction of water utilizing the coupled electro-dynamics–Langevin dynamics approach (43). The simulation assumed that the ends of the rod were each trapped by one of the two harmonic potential wells, with a viscous drag calculated under low Reynolds number condition (44). The simulation estimated the angular fluctuations as a function of the exposure time, as shown in Fig. 2B. Since the fluctuations were induced by thermal noise, shorter exposure times reduce the magnitude of the integrated fluctuations in the measurements.

Fig. 2C demonstrates the FWHM of the rocking curve measured from a $\sim 15\text{-}\mu\text{m}$ -long ZnO particle trapped at three different laser powers. The particle was trapped by two laser foci located $12\ \mu\text{m}$ apart (as shown in Fig. 2D). The natural width of the Bragg diffraction peak was determined to be $\sim 2.8\ \text{mrad}$. The distribution of the angular displacement in θ was about $0.9\ \text{mrad}$ FWHM at the full laser power. For a $\sim 15\text{-}\mu\text{m}$ -long ZnO rod, this angular fluctuation indicates that the FWHM of translational fluctuations of the ends of the rod was less than $14\ \text{nm}$. Given the $12\text{-}\mu\text{m}$ distance between the laser foci and the 0.9-mrad FWHM, the trapping stiffness was $0.40\ \text{pN/nm}$.

$\langle(\Delta\chi)^2\rangle$ is measured by directly observing the fluctuations of the vertical position of the diffraction peak. The vertical position of the peak was determined by fitting the intensity distribution to a Gaussian function. Before the measurement, the orientation of the trapped particle was optimized to maximize the intensity of the diffraction peak. As soon as the maximum intensity was achieved, the diffraction peak was measured as a function of time on an imaging detector at a 10-Hz sampling rate for more than $50\ \text{s}$ (Fig. 3A). The diffraction peak was found to initially oscillate in the vertical direction at $\sim 2\ \text{Hz}$ (as shown in Fig. 3B) and then stabilize after about $10\ \text{s}$. After stabilization, we observed a $\sim 0.3\text{-mrad}$ peak-to-peak fast fluctuation of the diffraction peak, as well as a slow drift of less than $0.1\ \text{mrad}$. Since the vertical position of the diffraction peak was directly related to the angular position of the particle in the χ direction, we determined the distribution of χ to be $0.19\ \text{mrad}$ FWHM, as shown in Fig. 3C. The resultant trapping stiffness was $8.9\ \text{pN/nm}$.

It may seem surprising that the angular stability in the χ direction ($0.19\ \text{mrad}$) is much better compared with that in the θ direction ($0.9\ \text{mrad}$); this means the trapping stiffness in the longitudinal direction of the laser beam is greater than in the transverse direction. This differential stability follows from the different sizes of the laser focus in the different directions of the standing-wave trap. As shown in Fig. 1B, the minimum diameter of the Gaussian focus in the transverse plane (i.e., x - z plane) is $0.64\ \mu\text{m}$ FWHM, limited by the numerical aperture of the microscope objective and the diffraction limit of the laser. In practice, this transverse width could be even larger as a result of other factors, such as phase aberrations introduced by the sample cell and optics. In contrast, the width of the standing-wave antinode is only $\sim 0.3\ \mu\text{m}$ FWHM in the longitudinal direction (i.e., y axis), resulting from the standing-wave interference in the counterpropagating OTs' geometry. Since the trapping stiffness is dictated by the gradient of the electric field, the larger transverse width of the focus results in a smaller trapping stiffness. The laser beam pointing fluctuations also affect the orientational stability in the transverse plane. This finding is consistent with our

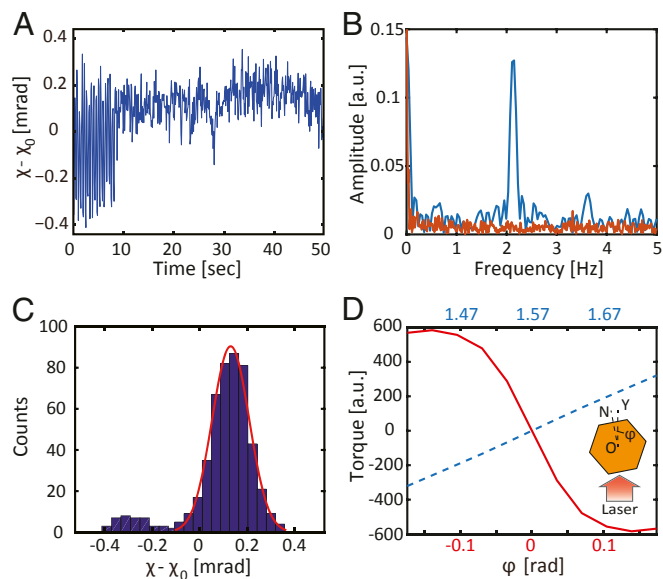


Fig. 3. Angular stability around x' and z' axes. (A) $\Delta\chi$ plotted as a function of time, measured at 10 Hz. (B) The spectrum obtained by Fourier transformation of the first 10 s of the time trace in A (blue) and the remaining 40 s after stabilization (red). (C) Histogram of the data in A. Counts at negative angles are from the oscillations in the first 10 s, while the positive angles are primarily due to the fluctuations after stabilization. The FWHM is 0.19 mrad. (D) Torque applied on a ZnO rod with a hexagonal cross-section when the laser is incident from the face (solid line) and the edge (dashed line) of the cross-section. OY is the laser incident direction, and ON is the normal direction of the facet of the rod. Both φ and the torque are defined as positive in the clockwise direction.

previous report that the fluctuations of nanoparticles in the antinodes of counterpropagating optical traps are much less than in single-beam geometries (32).

In our experiment, the particle could not be rotated in the φ direction due to its submicron diameter. Since the Q-vector of the [002] diffraction is parallel to the long axis of the rod, this rotation does not affect the diffraction angle. However, coherent diffraction is very sensitive to such rotation because it affects the orientation of the facets of the crystal. If the trapped rod were rotating around its long axis, the coherent fringes would either smear out or shift in time, depending on the rotational speed and the data acquisition rate. In our experiment, we did not observe rotation in φ . This is explained by the interaction between the laser and the prism-shaped particle. As shown in Fig. 3D, the cross-section of a ZnO crystalline particle is hexagonal (42, 45). The light scattering on the surfaces of the prism produces an optical force that can bias the crystal's alignment in φ . According to our finite-difference time-domain (FDTD) simulations, the prism is in equilibrium when either a facet or an edge faces the incident laser. When the laser is incident normal to the facet, any perturbation in φ induces a torque in the opposite direction, which will restore the φ angle to the equilibrium position. By comparison, when an edge of the prism is facing the incident laser, the equilibrium is unstable to small thermal fluctuations. Therefore, even though the φ angle of the ZnO rod cannot be adjusted to an arbitrary value, it only has minor angular fluctuations during the diffraction measurement.

Coherent Bragg Diffraction and Phase Retrieval of an Optically Trapped and Oriented Nanorod. We scanned the rocking curve of cylindrically shaped ZnO rods using the multifocus standing-wave optical trap. We will focus on the results for one particular ZnO rod that showed interesting structure in the reconstruction.

The two laser foci were 18 μm apart (Fig. 4A, *Inset*), and the X-ray beam was focused at the midpoint of the two laser foci. The isosurface of the 3D diffraction intensity in the vicinity of the Bragg peak is shown in Fig. 4A, and a slice of the diffraction peak is plotted in log scale in Fig. 4B. Given the spacing of the fringes, the diffraction originates from a crystal of a few hundred nanometer size in each dimension (i.e., a crystalline grain in the polycrystalline ZnO micron-scale rod).

The diffraction patterns of the target crystal were inverted by performing iterative phase retrieval (46). A partial coherence correction (47) was used to take into account the sample vibration effects. The phase retrieval was performed using the error reduction and hybrid input-output algorithms (46) with a guided approach (48), which is detailed in *Methods*. Both the 3D distribution of electron density and the 3D lattice displacement field projected along the [002] direction were reconstructed with 60-nm spatial resolution as defined by the phase retrieval transfer function (3, 49) (*SI Appendix, Fig. S4*). The resulting reconstructed image in Fig. 4C shows two crystalline grains, where the larger one is ~ 720 nm (x) \times 120 nm (y) \times 100 nm (z). The isosurfaces of the two grains are connected by a trench suggesting the location of the grain boundary. A slice at $x = 0$ shows the normalized amplitude and the phase of the hexagonal shape cross-section of the reconstructed crystal. Both the amplitude and the phase clearly show the grain boundary across the crystal. The phases and phase variations inside the two fragments are 1.24 ± 0.37 rad and -0.58 ± 0.24 rad, respectively, acquired by averaging the phase of all voxels in each fragment. The phases are relatively uniform inside the two grains as judged by the standard deviations. The 1.82 ± 0.44 -rad phase offset between the two fragments

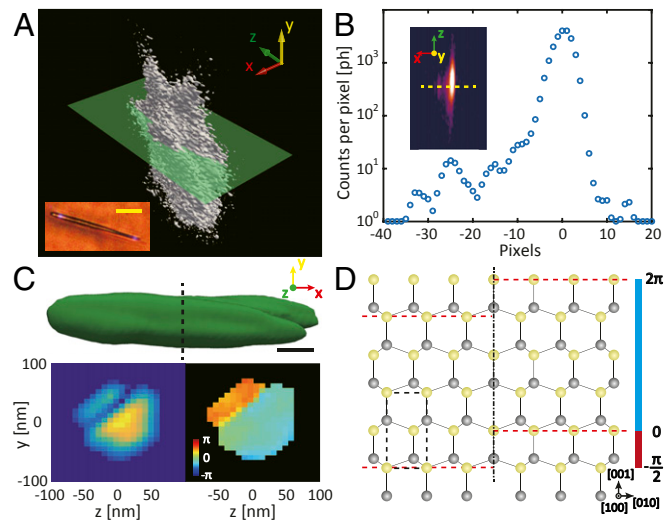


Fig. 4. CXDI of an optically trapped ZnO particle. (A) The diffraction intensity in reciprocal space from a ZnO particle shown in the *Inset*. The particle was trapped by two laser foci located 18 μm apart. The X-ray beam was focused at the middle point of the two laser foci. A slice of the diffraction peak (green plane) is shown in B, *Inset*. (Scale bar: 5 μm .) (B) Counts of photons in log scale along the yellow dashed line in the inset. (C, *Top*) The isosurface of the reconstructed crystalline grains. (Scale bar: 100 nm.) (C, *Bottom Left*) A slice of normalized amplitude at $x = 0$ of the reconstruction (dashed black line), which shows the hexagonally shaped cross-section of the crystal. (C, *Bottom Right*) The corresponding phase of the cross-section. (D) Lattice structures (Zn, yellow spheres; O, gray spheres) of the twinning crystalline grains. The black dashed box shows the unit cell of the ZnO wurtzite lattice. The red dashed lines indicate the lattice planes of [002] diffraction. The color bar demonstrates the $-\pi/2$ phase offset introduced by the deformation twinning along the [002] direction. The dashed-dotted black line shows the boundary between the twinning crystallographic domains.

indicates a lattice deformation along the Q-vector of the diffraction (i.e., the [002] direction). Both the continuous isosurface and the approximately $\pi/2$ phase shift suggest that this boundary is caused by a deformation twinning (as shown in Fig. 4D). The difference between the measured 1.82-rad and the $\pi/2$ (1.57-rad) phase offset could be caused by dislocation slip (50), which usually occurs simultaneously with deformation twinning.

Outlook and Applications. Our paper investigates the angular control and stability achievable with holographic OTs. We now discuss the factors that limit angular stability for Bragg CXDI and other potential applications. For Bragg CXDI measurements the required angular stability is dictated by the size of the features that need to be resolved. An estimate of the angular stability requirement is the speckle size θ_S , which is given by $\theta_S = \lambda/d$, where λ is the X-ray wavelength and d is the size of the crystal under the illumination of a coherent X-ray beam. Therefore, larger crystals require better angular stability. The angular stability of the trapped particle is defined by the probability distribution of the particle's angular displacement, which is dictated by the trapping stiffness, κ , and the spacing between the laser foci, D , as shown in Eq. 1. Many interrelated factors affect the trapping stiffness, including the wavelength and power of the trapping laser, the optical properties of the particle and the surrounding medium, the shape and size of the particle, and the performance of the optical system. For example, decreasing the wavelength and increasing the laser power usually result in a greater trapping stiffness due to the larger optical gradient; however, both are limited by the physical properties of the particle, such as the light reflectivity and absorption and, potentially, thermal damage. Conversely, the distance between the laser foci is only limited by the largest dimension of the particle, which is usually on a scale of 1 to 100 μm in 1D and 2D nanomaterials.

While we have demonstrated the ability to resolve the coherent diffraction from a 100-nm-scale crystalline grain in a micrometer-long cylindrically shaped particle, imaging a larger crystal using the conventional Bragg CXDI method would be more challenging due to the greater stability requirement. However, this limitation can be relaxed by reducing the size of the X-ray beam and performing Bragg ptychography (37) as described in *SI Appendix*. Compared with traditional Bragg CXDI, which requires the sample crystal to be smaller than the size of the coherent X-ray beam, Bragg ptychography is well-suited for measuring extended structures that are larger than the X-ray beam. Moreover, the recent development in phase retrieval algorithms that are able to reconstruct an object with dynamics considerably faster than the measurement times (51) is also a promising way to reduce the requirement of trapping stability.

Beyond taking advantage of new CXDI methods and algorithms, the performance of our apparatus can be improved with a shorter exposure time to minimize the smearing of the diffraction fringes (as shown in Fig. 2B). In our experiment, the minimum exposure time was 0.1 s due to the limited brilliance of the X-ray source. Owing to recent developments in high-flux-density X-ray sources like NSLS-II and APS Upgrade, this will be greatly improved ($\sim 100\times$) in the future. Moreover, optical and X-ray beamlines designed to minimize acoustic and mechanical noise will enhance the pointing stability of the optical and X-ray beams and further improve the performance.

Importantly, our optical goniometer method is useful not only for static measurements but can also be used to follow dynamics. The simple reconfigurability of the holographic OTs allowed us to observe an X-ray-induced morphology evolution of the trapped ZnO particles, including dissolution and surface deposition (*Movies S3–S5*). While the deposition did not affect the trapping stability, it did require adjustment of the laser foci to accommodate the significant length change due to the dissolution. However, relative to the subminute data collection time, such shape change was slow and

therefore did not affect the data collection. In the future, one may envision that the morphology evolution can be detected via real-time image recognition techniques and then compensated automatically by dynamically adjusting the holographic OTs. Since the refresh rate of an SLM (50 Hz or higher) is much faster than the data acquisition rate, this automatic compensation can maintain constant trapping stability for in situ Bragg CXDI studies.

Finally, the methodology we have developed has the potential for applications well beyond the CXDI community. With the holographic beam shaping technique, multiple laser foci with almost any configuration can be generated to match the samples' morphology. For example, it has been demonstrated that OTs can be utilized to manipulate biological samples for scanning X-ray fluorescence imaging (28) and Laue diffraction (29). For most X-ray microscopies such as scanning tomography and fluorescence imaging, our demonstrated magnitude of translational fluctuations is already much smaller than the size of the X-ray beam focus at most beamlines, which typically ranges from 0.5 to a few microns. As for X-ray diffraction microscopy, such as microcrystal crystallography, the demonstrated angular fluctuation is similar to or less than the width of the Bragg peaks. One potential limitation for applications lies in the laser-induced heating in the trapped sample, especially for biological samples. In our experiments, the temperature rise of the particle was estimated to be less than 10 K in the laser-illuminated sections and negligible in the X-ray illuminated section (*SI Appendix*). For samples that cannot tolerate a $<10\text{-K}$ temperature rise (e.g., those near a phase transition) additional controls such as cooling stages can be used to compensate the laser-induced temperature change.

Conclusion

Our work demonstrates that holographic optical trapping using a multifocus interferometric approach allows sufficient stability and angular resolution to perform as an “optical goniometer” for X-ray diffraction experiments. The holographic beam-shaping technique together with a specially designed sample cell can generate a multifocus standing-wave trap that is able to hold dielectric objects with high stability in a completely noncontact way. Cylindrically shaped ZnO particles, which are ~ 10 to 20 μm in length and submicron in diameter, can be precisely positioned and aligned in an aqueous environment. Translational fluctuations of the trapped particles of less than 20 nm and rotational fluctuations on the order of 100 μrad were demonstrated. Bragg coherent diffraction from a nanometer-scale crystalline grain inside a freely supported optically trapped ZnO particle, as well as the successful reconstruction, is also presented. The methodology demonstrated here provides an opportunity to perform in situ studies of lattice evolution in a suspended particle in solution phase, such as found in crystal growth and catalytic processes.

Methods

Compact Dynamic Holographic OTs. The schematic of the OTs setup and the corresponding laser path are shown in *SI Appendix, Fig. S3*. The optical trapping apparatus was built on a 12- \times 36-inch optical breadboard. No active or passive mechanical stabilization was used. The OTs used a 1,064-nm continuous-wave (CW) laser to manipulate micrometer-scale particles. The laser was generated by a single-mode linearly polarized CW ytterbium-doped fiber laser system (YLR-10-1064-LP; IPG Photonics). The phase of the laser beam was modified by a liquid-crystal SLM (HSPDM512-1064-DVI; Boulder Nonlinear Systems, Inc.). The diameter of the beam was adjusted to slightly overfill the liquid crystal chip of the SLM. A 4- f optical system was utilized to create a conjugate plane at the incident aperture of the microscope objective (UPLSAPO 60 \times water immersion; Olympus, N.A. = 1.2). For sample observation, the trapped particle was illuminated with incoherent white light and imaged onto a CCD camera by the same microscope objective and a lens. Two 1,064-nm laser line mirrors were utilized as dichroic mirrors to combine the white light beam and the IR laser. The laser power was adjusted by a pair of half-wave plates and polarizing beam splitter. The

maximum power measured at the back aperture of the microscope objective was 400 mW.

Sample Preparation. The sample consisted of ZnO tetrapod-shaped and cylindrically shaped particles (Pana-Tetra WZ-0501/WZ-0511/WZ-05F1; Panasonic Corp.). The length of the cylindrically shaped particles studied here was ~10 to 20 μm , while the diameter was ~0.5 to 1 μm . For each batch of the sample, 20 mg powder was mixed with 10 mL deionized (DI) water. The solution was then sonicated for 1 min to disperse the ZnO particles. To remove the small ZnO particles (length <5 μm), the mixture was centrifuged, and DI water was added to replace the top ~8 mL solution. This procedure was repeated three times to achieve the desired purity. Due to the small solubility of ZnO in water (52), a fresh sample was prepared daily to maintain a well-defined sample environment.

Microfluidic Sample Cell. As shown in *SI Appendix, Fig. S2*, a 500- μm (width) \times 100- μm (height) \times 35-mm (length) microfluidic channel and X-ray windows were etched on the surface of a Si wafer using Bosch RIE (Plasmalab 100; Oxford Instruments). Several "islands" were made in the center area of the microfluidic channel. A 100-nm-thick gold film was sputtered on the center area of the channel as a mirror. Then, anodic bonding between a 150- μm Pyrex wafer and the 500- μm Si wafer was conducted via a homemade tool. The sample cell was then connected to silicone rubber tubing via adapters made by 3D printing and sealed by epoxy. A syringe pump was utilized to control the fluid flow. During the experiments, the sample cell was mounted with the Pyrex side facing downward. The particles could be trapped either below the ceiling surface or below the top of the "islands." Since the water flow could perturb the trapped particle, the syringe pump was turned off during the X-ray diffraction measurements.

The flow cell was mounted horizontally on a three-axis goniometer using 3D-printed holders. It was aligned parallel to the X-ray beam by observing the transmitted X-rays via a downstream optical camera. A piece of yttrium-aluminum-garnet crystal was placed in front of the camera to convert the X-ray photons into visible light. The laser beam, which was aligned to propagate upward along the normal direction of the surface of the sample cell, transmitted through the Pyrex wafer and then was reflected by the gold mirror, forming a standing-wave trap located several microns below the surface of the gold.

Measurement of X-Ray Diffraction. The experiment was performed at Beamline 34-ID-C of the Advanced Photon Source at Argonne National Laboratory. The coherent X-ray beam was focused into an approximate 1.0- (H) \times 0.8- (V) μm^2 spot by Kirkpatrick-Baez mirrors and propagated through the microfluidic sample cell (as shown in *SI Appendix, Fig. S2*). The photon energy was adjusted to 9 keV to maximize the transmitted flux. The diffraction was collected by a Medipix2/Timepix detector with 256 \times 256 of 55- \times 55- μm^2 pixels. Owing to the limited vertical aperture of the sample cell, the incident and diffracted X-ray beams were in the x - z plane, where z was the downstream direction and x was the outboard direction. For the Bragg CXDI measurement, the particle was rotated by the OTs around the vertical axis (y' axis) to scan the rocking curve. A total 1° angular range centered at the Bragg peak was scanned with a 0.02° step using 1-s exposure time per step. For the angular stability studies, 0.1-s exposure time per frame was used.

X-Ray Diffraction Simulation. The intensity of the diffraction pattern obtained from the ZnO crystal is determined by the square of the crystal form factor,

$$F^{\text{crys}}(\vec{Q}) = f^0(\vec{Q}) \cdot F^{\text{latt}}(\vec{Q}),$$

where $f^0(\vec{Q})$ is the atomic form factor and $F^{\text{latt}}(\vec{Q})$ is the lattice sum. The atomic form factor was calculated for ZnO using the Herman-Skillman Hartree-Fock-Slater self-consistent atomic field program (53). The lattice sum was determined by a summation across the crystal lattice vectors and offset vectors associated with the ZnO wurtzite lattice (54).

The diffraction peak was simulated by calculating the probability of observing a scattering event per unit solid angle, which is represented as the scattering differential cross-section (55),

$$\frac{1}{r_e^2} \frac{d\sigma}{d\Omega} = [1 - \cos^2(\chi) \sin^2(\theta)] |F^{\text{crys}}|^2,$$

where r_e is the classical electron radius and θ and χ denote the angular displacement in the polar and azimuthal directions, respectively. There-

fore, the number of photons in an area $\sin(\theta)d\theta d\chi$ located at the angles (θ, χ) is

$$dP = \frac{d\sigma}{d\Omega} \cdot \frac{N}{A} \sin(\theta) d\theta d\chi,$$

where N is the total number of photons and A is the cross-section area of the X-ray beam (i.e., the number of photons scattered per differential solid angle).

Electrodynamics Simulation. The electromagnetic field of the standing-wave trap and the optical force applied on the ZnO rod were calculated using Lumerical FDTD Solution software. The ZnO rod (hexagonal prism shape refractive index 1.94) was assumed to be immersed in water (refractive index 1.33) and illuminated by two focused 1,064-nm-wavelength linearly polarized Gaussian beams with a N.A. = 1.2. A 100-nm-thick Au film was placed in the downstream direction of the ZnO rod. To reduce the amount of simulation time, the distance between the ZnO rod and the Au film was set to 3 μm . The two Gaussian beams had different focal lengths. The beam with a shorter focal length was focused on the particle directly, while the other one was reflected by the Au film and then focused on the particle. The ZnO rod was placed in the x - z plane and light propagated along the y direction (Fig. 1). The optical forces were calculated by integrating the Maxwell stress tensor over a surface surrounding the particle. To map the optical force in three dimensions, the ZnO rod was moved around the equilibrium position (the center of the strongest antinode of the standing wave) with a displacement less than 200 nm.

Brownian Motion Simulation. The motion of the trapped ZnO rod was simulated by calculating the Langevin dynamics of the particle in a time sequence utilizing the BAOAB scheme (43). In optical trapping, the trapped particle can be considered as residing in a harmonic potential well if its fluctuations are small in comparison with the size of the laser focus. The electrodynamic simulation demonstrates that the optical trap in our experiment acts as a harmonic potential well if the positional fluctuations of the trapped ZnO are less than 100 nm. Therefore, the optical force was simply calculated by multiplying the displacement with the trapping stiffness obtained from the electrodynamic simulation. Because the Reynolds number was low, the viscous drag was calculated by solving the Stokes equations for long, slender particles (44). The motion of the trapped rod was calculated in each time step (typically 10^{-6} s) over a 1-s period of time, and the angular fluctuation was determined by fitting the histogram of the angular positions to a Gaussian function.

Coherent Diffraction Imaging Phase Retrieval. The coherent diffraction pattern was inverted using an iterative phase retrieval algorithm in a guided approach (48). The raw data were thresholded by setting intensities below two photons to zero. Five generations, each including five independent reconstructions, were used for the guided algorithm. The measured data with a random phase were used as the starting point of the reconstructions in the first generation. In each generation, the best reconstruction was chosen according to the lowest error metric and used as the seed for the next generation. Iterations were done by alternating between error reduction (ER) and hybrid input-output (HIO) with 10 iterations of ER followed by 40 iterations of HIO for 150 total iterations. The algorithms were initialized with a support box filled with a constant real density. Shrinkwrap (56) was implemented to improve the support starting at iteration 50 and updating every five iterations. A partial coherence correction was used to determine a mutual coherence function. The best reconstruction from the last generation was chosen as the result.

ACKNOWLEDGMENTS. We thank the staff of the APS 34-ID-C beamline, in particular Evan Maxey and Dr. Jörg Maser, for their support prior to and during the synchrotron experiments; Dr. David Grier for his advice in holographic beam shaping; Drs. Ralu Divan, Liliana Stan, Michael Wojcik, and Kamleshkumar Suthar for their contribution in sample cell fabrication; and Drs. Xianbo Shi and Hanfei Yan for helpful discussions. This work was supported by the US Department of Energy (DOE), Office of Science, Basic Energy Sciences, Chemical Sciences, Geosciences, and Biosciences Division through Argonne National Laboratory (Y.G., S.H.S., P.J.H., and L.Y.) and the Vannevar Bush Faculty Fellowship program sponsored by the Basic Research Office of the Assistant Secretary of Defense for Research and Engineering and funded by the Office of Naval Research Grant N00014-15-1-0027 (Z.Y., Y.Y., N.S., and N.F.S.). Use of the Center for Nanoscale Materials (CNM) and Advanced Photon Source (APS), both Office of Science user facilities, was supported by the US DOE, Office of Science, Office

of Basic Energy Sciences, under Contract DE-AC02-06CH11357. X-ray diffraction data were collected at the Microdiffraction and Coherent X-ray Scattering Beamline 34-ID-C at APS; microfluidic cell fabrication and electrostatic simulations on the HPC Carbon cluster were performed at

CNM. X-ray diffraction data analysis was partially supported by National Synchrotron Light Source II, a US DOE Office of Science User Facility operated for the DOE Office of Science by Brookhaven National Laboratory under Contract DE-SC0012704 (to Y.G. and X.H.).

- Miao JW, Charalambous P, Kirz J, Sayre D (1999) Extending the methodology of X-ray crystallography to allow imaging of micrometre-sized non-crystalline specimens. *Nature* 400:342–344.
- Miao J, et al. (2003) Imaging whole *Escherichia coli* bacteria by using single-particle x-ray diffraction. *Proc Natl Acad Sci USA* 100:110–112.
- Chapman HN, et al. (2006) High-resolution ab initio three-dimensional x-ray diffraction microscopy. *J Opt Soc Am A Opt Image Sci Vis* 23:1179–1200.
- Chapman HN, Nugent KA (2010) Coherent lensless X-ray imaging. *Nat Photonics* 4: 833–839.
- Miao J, Ishikawa T, Robinson IK, Murnane MM (2015) Beyond crystallography: Diffractive imaging using coherent x-ray light sources. *Science* 348:530–535.
- Emma P, et al. (2010) First lasing and operation of an angstrom-wavelength free-electron laser. *Nat Photonics* 4:641–647.
- Ishikawa T, et al. (2012) A compact X-ray free-electron laser emitting in the sub-angstrom region. *Nat Photonics* 6:540–544.
- Popmintchev T, et al. (2009) Phase matching of high harmonic generation in the soft and hard X-ray regions of the spectrum. *Proc Natl Acad Sci USA* 106:10516–10521.
- Chapman HN, et al. (2006) Femtosecond diffractive imaging with a soft-X-ray free-electron laser. *Nat Phys* 2:839–843.
- Sandberg RL, et al. (2007) Lensless diffractive imaging using tabletop coherent high-harmonic soft-X-ray beams. *Phys Rev Lett* 99:098103.
- Jiang H, et al. (2010) Quantitative 3D imaging of whole, unstained cells by using X-ray diffraction microscopy. *Proc Natl Acad Sci USA* 107:11234–11239.
- Nelson J, et al. (2010) High-resolution x-ray diffraction microscopy of specifically labeled yeast cells. *Proc Natl Acad Sci USA* 107:7235–7239.
- Seibert MM, et al. (2011) Single mimivirus particles intercepted and imaged with an X-ray laser. *Nature* 470:78–81.
- Ekeberg T, et al. (2015) Three-dimensional reconstruction of the giant mimivirus particle with an x-ray free-electron laser. *Phys Rev Lett* 114:098102.
- Kurta RP, et al. (2017) Correlations in scattered X-ray laser pulses reveal nanoscale structural features of viruses. *Phys Rev Lett* 119:158102.
- Neutze R, Wouts R, van der Spoel D, Weckert E, Hajdu J (2000) Potential for biomolecular imaging with femtosecond X-ray pulses. *Nature* 406:752–757.
- Pfeifer MA, Williams GJ, Vartanyants IA, Harder R, Robinson IK (2006) Three-dimensional mapping of a deformation field inside a nanocrystal. *Nature* 442:63–66.
- Robinson IK, Vartanyants IA, Williams GJ, Pfeifer MA, Pitney JA (2001) Reconstruction of the shapes of gold nanocrystals using coherent x-ray diffraction. *Phys Rev Lett* 87: 195505.
- Williams GJ, Pfeifer MA, Vartanyants IA, Robinson IK (2003) Three-dimensional imaging of microstructure in Au nanocrystals. *Phys Rev Lett* 90:175501.
- Hruszkewycz SO, et al. (2018) Strain annealing of SiC nanoparticles revealed through Bragg coherent diffraction imaging for quantum technologies. *Phys Rev Mater* 2: 086001.
- Robinson I, Harder R (2009) Coherent X-ray diffraction imaging of strain at the nanoscale. *Nat Mater* 8:291–298.
- Kim D, et al. (2018) Active site localization of methane oxidation on Pt nanocrystals. *Nat Commun* 9:3422.
- Lo YH, et al. (2018) In situ coherent diffractive imaging. *Nat Commun* 9:1826.
- Liu C, Kawana M, Song D, Ruppel KM, Spudich JA (2018) Controlling load-dependent kinetics of β -cardiac myosin at the single-molecule level. *Nat Struct Mol Biol* 25: 505–514.
- Huang R, et al. (2011) Direct observation of the full transition from ballistic to diffusive Brownian motion in a liquid. *Nat Phys* 7:576–580.
- Summers MD, Burnham DR, McGloin D (2008) Trapping solid aerosols with optical tweezers: A comparison between gas and liquid phase optical traps. *Opt Express* 16: 7739–7747.
- Shvedov VG, et al. (2010) Optical vortex beams for trapping and transport of particles in air. *Appl Phys A* 100:327–331.
- Vergucht E, et al. (2015) In vivo X-ray elemental imaging of single cell model organisms manipulated by laser-based optical tweezers. *Sci Rep* 5:9049.
- Santucci SC, et al. (2011) Optical tweezers for synchrotron radiation probing of trapped biological and soft matter objects in aqueous environments. *Anal Chem* 83: 4863–4870.
- Nicolas J-D, Hagemann J, Sprung M, Salditt T (2018) The optical stretcher as a tool for single-particle X-ray imaging and diffraction. *J Synchrotron Radiat* 25:1196–1205.
- Bowman R, et al. (2011) Position clamping in a holographic counterpropagating optical trap. *Opt Express* 19:9908–9914.
- Yan Z, Bao Y, Manna U, Shah RA, Scherer NF (2014) Enhancing nanoparticle electrostatics with gold nanoplate mirrors. *Nano Lett* 14:2436–2442.
- Eaton SW, Fu A, Wong AB, Ning C-Z, Yang P (2016) Semiconductor nanowire lasers. *Nat Rev Mater* 1:16028.
- LaPierre RR, Robson M, Azizur-Rahman KM, Kuyanov P (2017) A review of III–V nanowire infrared photodetectors and sensors. *J Phys D Appl Phys* 50:123001.
- Ertekin E, Greaney PA, Chrzan DC, Sands TD (2005) Equilibrium limits of coherency in strained nanowire heterostructures. *J Appl Phys* 97:114325.
- Eshelby JD (1953) Screw dislocations in thin rods. *J Appl Phys* 24:176–179.
- Hill MO, et al. (2018) Measuring three-dimensional strain and structural defects in a single InGaAs nanowire using coherent X-ray multiangle Bragg projection ptychography. *Nano Lett* 18:811–819.
- Sun Y, et al. (2012) Ambient-stable tetragonal phase in silver nanostructures. *Nat Commun* 3:971.
- Sanchez AM, et al. (2018) Stable defects in semiconductor nanowires. *Nano Lett* 18: 3081–3087.
- Dienierowitz M, Mazilu M, Dholakia K (2008) Optical manipulation of nanoparticles: A review. *J Nanophotonics* 2:021875.
- Montes-Usategui M, Pleguezuelos E, Andilla J, Martín-Badosa E (2006) Fast generation of holographic optical tweezers by random mask encoding of Fourier components. *Opt Express* 14:2101–2107.
- Kolodziejczak-Radzimska A, Jesionowski T (2014) Zinc oxide—from synthesis to application: A review. *Materials (Basel)* 7:2833–2881.
- Sule N, Rice SA, Gray SK, Scherer NF (2015) An electrostatics-Langevin dynamics (ED-LD) approach to simulate metal nanoparticle interactions and motion. *Opt Express* 23:29978–29992.
- Guyon E, Nadal JP, Pomeau Y, eds (2012) *Disorder and Mixing: Convection, Diffusion and Reaction in Random Materials and Processes*. (Springer, Berlin).
- Leake SJ (2010) Coherent X-ray diffraction imaging of zinc oxide crystals. PhD thesis (Univ College London, London). Available at https://www.ucl.ac.uk/~ucapikr/theses/Leake_PhDthesis_2010.pdf.
- Fienup JR (1982) Phase retrieval algorithms: A comparison. *Appl Opt* 21:2758–2769.
- Clark JN, Huang X, Harder R, Robinson IK (2012) High-resolution three-dimensional partially coherent diffraction imaging. *Nat Commun* 3:993.
- Chen C-C, Miao J, Wang CW, Lee TK (2007) Application of optimization technique to noncrystalline x-ray diffraction microscopy: Guided hybrid input-output method. *Phys Rev B Condens Matter Mater Phys* 76:064113.
- Tripathi A, et al. (2011) Dichroic coherent diffractive imaging. *Proc Natl Acad Sci USA* 108:13393–13398.
- Huang X, et al. (2015) Deformation twinning of a silver nanocrystal under high pressure. *Nano Lett* 15:7644–7649.
- Clark JN, Huang X, Harder RJ, Robinson IK (2014) Dynamic imaging using ptychography. *Phys Rev Lett* 112:113901.
- David CA, et al. (2012) Dissolution kinetics and solubility of ZnO nanoparticles followed by AGNES. *J Phys Chem C* 116:11758–11767.
- Herman F, Skillman S (1963) *Atomic Structure Calculations* (Prentice Hall, Upper Saddle River, NJ).
- Morkoç H, Özgür Ü (2009) *Zinc Oxide: Fundamentals, Materials and Device Technology* (Wiley-VCH, Weinheim, Germany).
- Hubbell JH, et al. (1975) Atomic form factors, incoherent scattering functions, and photon scattering cross sections. *J Phys Chem Ref Data* 4:471–538.
- Marchesini S, et al. (2003) X-ray image reconstruction from a diffraction pattern alone. *Phys Rev B* 68:140101.